Available online at www.sciencedirect.com

jmr&t Journal of Materials Research and Technology

journal homepage: www.elsevier.com/locate/jmrt

Original Article

Influences of strain rate, Al concentration and grain heterogeneity on mechanical behavior of $CoNiFeAl_xCu_{1-x}$ high-entropy alloys: a molecular dynamics simulation

Luling Wang [a], *Weitao Liu* [a], *Binyin Zhu* [a], *Wei Chen* [a], *Feng Zhang* [a,c], *Bin Liu* [a], *Jingli Liu* [a], *Jianqiu Zhou* [a,d,*], *Yonghao Zhao* [b,**]

[a] *Department of Mechanical Engineering, Nanjing Tech University, Nanjing, Jiangsu, 210009, China*
[b] *Nano and Heterogeneous Materials Center, School of Materials Science and Engineering, Nanjing University of Science and Technology, Nanjing, 210094, China*
[c] *School of Mechanical Engineering, Nanjing Institute of Technology, Nanjing, Jiangsu, 211167, China*
[d] *School of Mechatronics Engineering, Guizhou Minzu University, Guiyang, Guizhou, 550025, China*

ARTICLE INFO

Article history:
Received 26 March 2021
Accepted 25 July 2021
Available online 29 July 2021

Keywords:
Molecular dynamics simulation
High-entropy alloys
Strain rate
Al concentration
Nano-scale dislocation slip
Heterogeneous grain structure

ABSTRACT

High-entropy alloys (HEAs) with a heterogeneous grain structure have been revealed to possess excellent combination of strength and toughness. However, the atomic-level deformation mechanisms of the heterogeneous HEAs were not reported yet. In this work, physical models were constructed based on the experimental observation and atomic simulations are performed to investigate the tensile behavior of face centered cubic (FCC) heterogeneous $CoNiFeAl_xCu_{1-x}$ HEAs at different strain rates (5×10^7–1×10^{10} s^{-1}), Al concentration (x = 0.1, 0.2, 0.3 and 0.4) and degrees of grain heterogeneity. Result analysis reveals the multiple deformation mechanisms including dislocation motion, diffusion from grain interior to grain boundary and stacking faults (SFs) as well as their interaction. The strain rates seriously influence the body centered cubic (BCC) transformation from FCC in the large grains. Besides, with the reduction of Al concentration, the value of stable stacking fault energy (SFE) raises, while the tensile yield stress increases. Finally, increasing the large grain size (D_G) of the heterogeneous grain structure improved the plasticity due to the combination of enhanced FCC to BCC phase transformation and high uniform ductility of large grains. This work provides a micromechanical understanding for designing the excellent mechanical property of HEAs by optimizing material structure parameters of heterogeneous grain structure HEAs.

* Corresponding author.
** Corresponding author.
E-mail addresses: zhouj@njtech.edu.cn (J. Zhou), yhzhao@njust.edu.cn (Y. Zhao).
https://doi.org/10.1016/j.jmrt.2021.07.116

1. Introduction

Different from traditional alloys, high-entropy alloys (HEAs), also known as multi-component alloys proposed in 2004 by Ye et al. [1] and Cantor et al. [2], respectively, are composed of more than five major elements [3–11]. HEAs exhibit excellent mechanical potentials, such as outstanding thermal stability [12], great fatigue resistance properties [13,14], ultra-high strength and hardness as well as fracture toughness at both room temperature [15,16] and ultralow temperature [17]. These excellent properties revealed the great potential of HEAs as powerful functional materials.

To solve the problem that both high strength and good ductility cannot be achieved simultaneously in nanocrystalline materials, many researchers have tried to construct heterogeneous structures to solve this contradiction. Wang et al. [18] synthesized heterogeneous grain structure Cu. They found that the tensile ductility could reach 60% due to the large grains preferentially adapting to deformation. An increasing number of researchers have synthesized HEAs with heterogeneous structure recently. For instance, Wu et al. [16] designed the HEA with a heterogeneous grain structure, which possesses a uniform elongation of 30%, yield strength of 711 MPa and a tensile strength of 928 MPa. Schuh et al. [19] explored the feasibility of CoCrFeMnNi and its high-performance subvariant CrCoNi in designing bimodal microstructures to obtain excellent mechanical properties. In contrast, CrCoNi alloy was easier to form a bimodal microstructure. After annealing at 500 °C for 100 h, a combination of high tensile strength of 1500 MPa and 10% elongation at break was obtained. John et al. [20] found that the $AlCoCrFeNi_{2.1}$ eutectic high-entropy alloy (EHEA) showed a high fracture strength of 2225 MPa, mainly related to heterogeneous structure and various strengthening mechanisms. Although the deformation mechanism of pure metal, binary alloys with heterogeneous grain size distribution has been studied extensively in some previous experiments, the atomic-level deformation mechanisms and mechanical behavior of HEAs with the heterogeneous structure were never reported.

Molecular dynamics (MD) simulation of HEAs is still challenging because most of the interaction potentials between elements cannot be obtained accurately up to now. Nevertheless, in the past few years, there are still several reports on MD simulation of HEAs after a few suitable potentials were discovered [21–26]. Lin et al. [26] reported the MD simulation of radiation tolerance of Ni–Co–Cr–Fe HEA, which provides a significant reference for the engineering design of nickel-based HEA for radiation tolerance applications. Li et al. [22] provided a reliable explanation for the transformation-induced plasticity (TRIP) and phase transformation mechanisms of nanocrystalline FeMnCoCr HEAs by MD simulation. Moreover, Chen et al. [27] found the cross value of the Hall–Petch and inverse Hall–Petch relations of FCC $CoNiFeAl_{0.3}Cu_{0.7}$ and BCC $CoNiFeAl_{0.7}Cu_{0.3}$ HEAs by MD. Afkham et al. [23] studied the mechanical properties of AlCrCoFeCuNi HEA at different temperatures. They found that a high free volume was obtained in the sample rich in aluminum atoms.

In this work, the FCC heterogeneous grain structured $CoNiFeAl_xCu_{1-x}$ HEAs were constructed in MD simulations. Uniaxial tensile simulations were performed to investigate the tensile behavior. The methods of model construction and calculation are introduced in Section 2. The effects of different strain rates, Al concentration and large grain size on tensile mechanical properties of the alloys were sequentially explored in Section 3. Finally, the conclusions are summarized in Section 4.

2. MD simulation details

$CoNiFeAl_xCu_{1-x}$ HEA with a heterogeneous grain size distribution was generated by the open-source code LAMMPS [28]. The visualization software OVITO was used to analyze the final simulation results [29]. Fu et al. [30] fabricated nanocrystalline and ultrafine grained FCC $CoNiFeAl_{0.3}Cu_{0.7}$ HEA (cf. Fig. 1a). Based on this experimental observation, the physical models were built according to the following processes. The Voronoi tessellation method was applied to generate the polycrystal of Co. Before the large single crystal was inserted into the model, the simulation cells were composed of 70 small grains with mean grain size of 9 nm as the small grain region. Then, we deleted the atoms in the sphere with a certain diameter from the center of the box and then filled the deleted sphere with a single crystal. Here, we simplified the physical model shown in the experimental observation, for the large grains, spherical grains were used to represent them. Finally, Ni, Fe, Al and Cu atoms were randomly replaced with Co to construct the HEA structures (cf. Fig. 1b). Fig. 1c is the common neighbor analysis. Mean cohesive energy per atom as a function of lattice constant for $CoNiFeAl_{0.3}Cu_{0.7}$ is presented in Fig. 1d. The calculated equilibrium lattice constant is about 3.6 Å, which is quite consistent with the experimental value of 3.598 Å [30]. Besides, the diameter of the sphere in the center D_G was regarded as large grain region and a significant factor affecting the mechanical properties. Therefore, simulation cells with various D_G ($D_G = 0$, 12, 14, 16, 18, 20, 22, 24 and 26 nm) were built in this work. The dimensions of the model were $30 \times 30 \times 30$ nm^3 with the initial FCC lattice constant 3.598 Å (about 2,300,000 atoms in total).

The embedded-atom method (EAM) potential developed by Zhou et al. [31,32] was adopted to describe the interaction between Co–Ni–Fe–Al–Cu system. The following function can express the total energy of $CoNiFeAl_xCu_{1-x}$ HEA [33]:

$$E_{tot} = \frac{1}{2}\sum_{i \neq j}\varphi_{\alpha\beta}(r_{ij}) + F_{\alpha}\left(\sum_{i \neq j}\rho_{\alpha}(r_{ij})\right) \quad (1)$$

where r_{ij} is the distance of neighboring atoms, is the pair potential, α and β are neighboring atoms, ρ_α is the value of the electron charge density generated by the atom j of type α at the position of atom i. F_α is an embedding function, which represents the energy required to embed the atom i of type α in the electron cloud. This potential has previously been applied to MD simulations of some HEAs systems. Li et al. [22] found that the error of the yield strength between simulation and the experimental values deformed at a strain rate of 5×10^6 s^{-1} is only 4%.

In this work, periodic boundary conditions were enforced along x, y and z direction. The simulations were energy-minimized by performing the conjugate gradient (CG) algorithm and the final energy convergence was 10^{-12}. Before performing the tensile loading, a hybrid Monte Carlo (MC)/Molecular Dynamics (MD) relaxation was used to relax initial

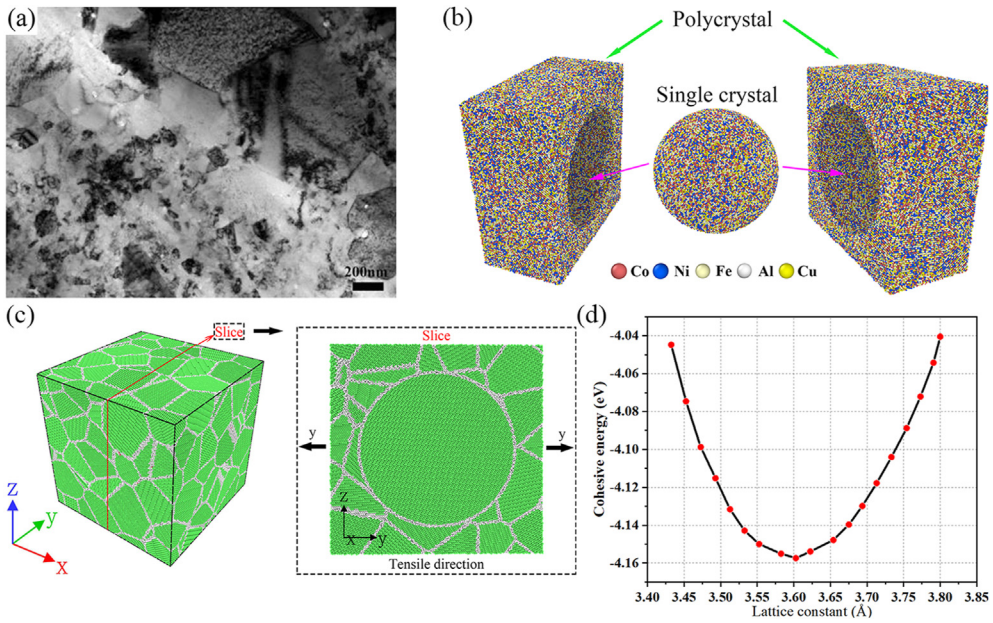

Fig. 1 – FCC heterogeneous grain structured $CoNiFeAl_{0.3}Cu_{0.7}$ HEA [30]; (a) The TEM image showing ultrafine grains and nanocrystalline grains; (b) Atomic type and structure; (c) Common neighbor analysis and (d) The evolution of mean cohesive energy per atom as a function of lattice constant.

system. The hybrid relaxation with 1000 times of swaps every 1 ps for a total 200 ps was performed in isothermal-isobaric NPT ensemble at 300 K and zero external pressure. This relaxation method is suitable for multi-principal component alloys for a relatively stable initial structure can be found [34,35]. After the systems were thermally balanced, uniaxial tensile simulations with different strain rates (5×10^7, 1×10^8, 1×10^9 and 1×10^{10} s^{-1}) along direction y were performed. During the tensile simulations, the temperature was set as 300 K, and the external stress tensor was set to be zero in the x and z direction.

3. Results

3.1. *Tensile deformation mechanism at different strain rates*

The tensile stress–strain curves at four strain rates (5×10^7, 1×10^8, 1×10^9 and 1×10^{10} s^{-1}) are presented in Fig. 2a and the yield stress is 1.628, 1.737, 1.979 and 2.827 GPa, respectively. According to the curve corresponding to the strain rate of 1×10^{10} s^{-1}, the elastic stage is indicated by the black dotted line. After $\varepsilon = 0.01$, the curve deviates from the linear elastic stage and shows sharp strain hardening in a very short strain range. However, the strain–stress curves harden in a larger strain range in experiments [36,37]. The difference between experiment and MD simulation can be attributed to the stress overshoot phenomenon caused by the high strain rate used in the MD simulation [38].

The deformation processes are shown in Fig. 3. At the initial stage of deformation ($\varepsilon = 4.5\%$), dislocations have already propagated into large grains and annihilated at the opposite grain boundary (GB) at the strain rate of 5×10^7 s^{-1} (cf. Fig. 3a). It can be seen from Fig. 3a that the alloy has already undergone about 3% plastic deformation after yielding. By contrast, only a small part of dislocations has

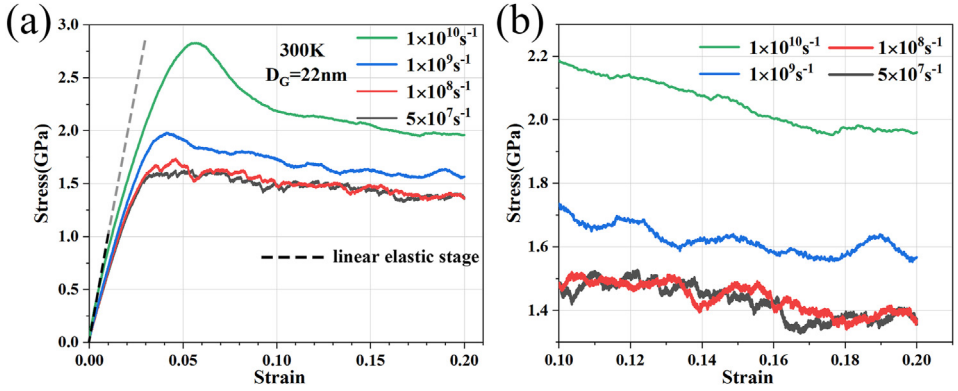

Fig. 2 – (a) Stress–strain curve of the heterogeneous grain structured $CoNiFeAl_{0.3}Cu_{0.7}$ HEA under different strain rates; (b) Enlarged curve of plastic deformation stage.

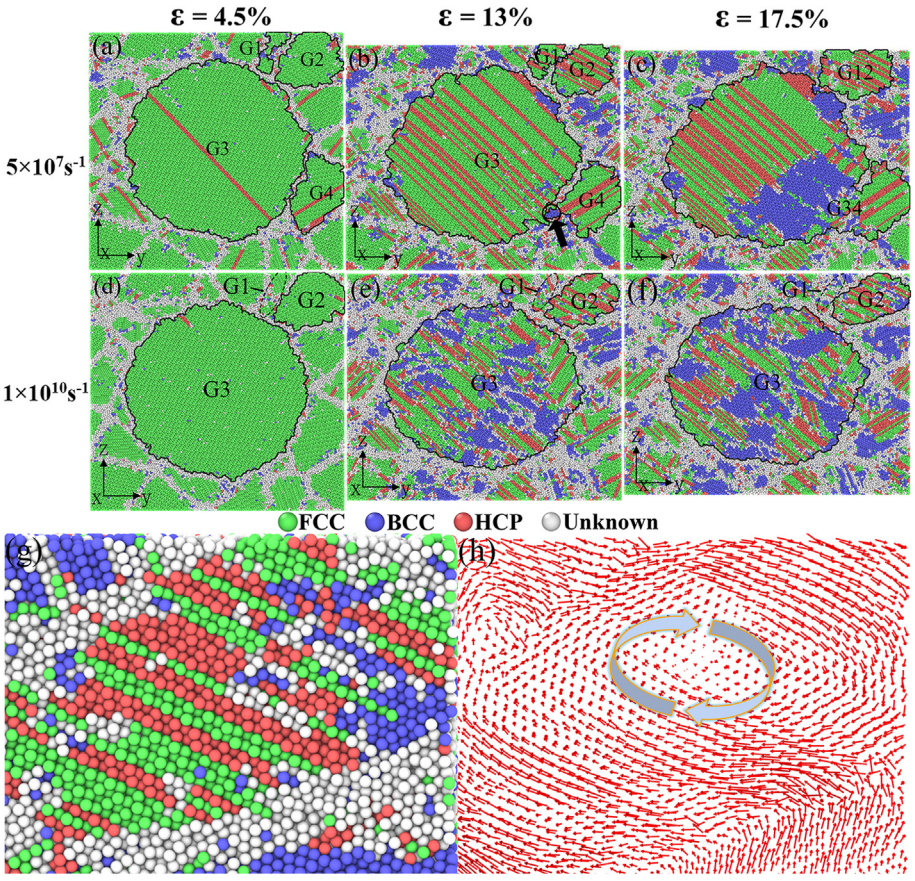

Fig. 3 – Deformation process of heterogeneous grain structured $CoNiFeAl_{0.3}Cu_{0.7}$ HEA with $D_G = 22$ nm under 300 K and different strain rates: (a)–(c) Strain rate is 5×10^7 s^{-1}; (d)–(f) Strain rate is 1×10^{10} s^{-1}; (g) Grain G2 under 1×10^{10} s^{-1} and $\varepsilon = 17.5\%$; (h) Displacement vectors of grain G2.

been injected into the grains (whether large or small grains) at the strain rate of $1 \times 10^{10} s^{-1}$ (cf. Fig. 3d). Because the alloy has just undergone a transition from linear elastic stage to non-linear elastic stage near the strain of 4% (cf. Fig. 2a), an increasing number of grains begin to yield with dislocations emitted from GBs and propagated into the large grain interior (cf. Fig. 3d). Moreover, some disordered atoms have appeared in grain G1 (cf. Fig. 3d), which indicates that atoms of grain interior have become unstable. Therefore, according to the Masing hardening [39], the strain hardening rate gradually drops with the hardening decay of the yielded grains.

At the strain rate of 1×10^{10} s^{-1}, the intersected SFs are formed by the dislocations passing through the pre-formed SFs when $\varepsilon = 13\%$ (cf. Fig. 3e). In this case, the intersected SFs become the dislocation barrier, which increases flow stress at high strain rates (cf. Fig. 2b) [40]. As the deformation continues (cf. Fig. 3e and f), the previously generated dislocation and SFs provided a diffusion path for GB atoms to diffuse into grain G1 [41]. When $\varepsilon = 17.5\%$ (cf. Fig. 3f), plenty of atoms become disordered in grain G1 with the indistinguishable grain outline. Besides, the atomic displacement vector of grain G2 shows a movement trend as indicated by the red arrows (cf. Fig. 3g and h), and the shape of grain G2 has been changed a lot. Based on these phenomena, it demonstrates that grain rotation happens to grain G2. At the strain rate of 5×10^7 s^{-1}, the previous grains G1, G2, G3 and G4 (cf. Fig. 3a and b) combine into two new grains G12 and G34 (cf. Fig. 3c) via grain rotation. However, there is no conspicuous grains combination at the strain rate of 1×10^{10} s^{-1} (cf. Fig. 3d–f). When the nanocrystalline materials are subjected to loads, inconsistent deformation in heterogeneous grain structure results in the increased net torque between adjacent grains. Therefore, the dislocations are multiplied to form strain field, and extra geometrically necessary dislocations (GNDs) accumulate near the GB [42]. From the viewpoint of energy and mechanics, dislocation activity is beneficial to grain rotation. The back stress and grain rotation have similarities in multiplying dislocations to improve mechanical properties, especially plasticity. According to back stress theory, lots of dislocations pile up near the boundary of soft large grains to sustain more strain. If the interface between large and small grains is regarded as critical region, the farther away from this region, the forward stress and back stress will become weaker. Stimulated by the forward stress and back stress, the extra GNDs evolve in the form of grain rotation to accommodate mechanical incompatibility. Besides, away from the critical region, the weakening of the front and back stress lead to the reduction of GNDs, resulting in the subsequent weakening of grain rotation. However, the grain size is much smaller than that in the experiments due to the three-dimensional size

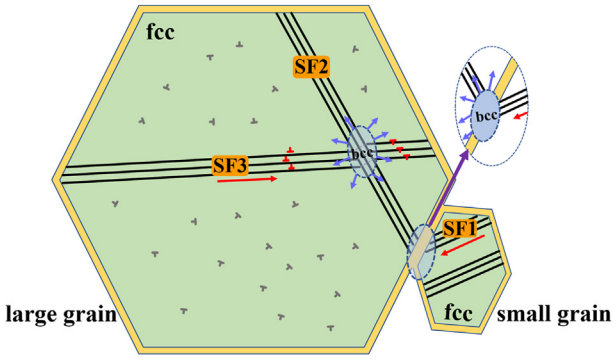

Fig. 4 – Schematic representation of FCC to BCC phase transformation behavior in HEA with heterogeneous grain structure.

limitation in MD. Therefore, to systematically study the deformation behavior with obvious strain gradient, the two-dimensional model may be more suitable, which is worth further exploration in the future.

It is worth noting that the FCC to BCC phase transformation almost always starts from the GBs in the large grain when the strain rate is 5×10^7 s^{-1}, while at the strain rate of 1×10^{10} s^{-1}, phase transformation appears both at GBs and grain interiors. Besides, the degree of phase transformation in the large grain is significantly increased at high strain rate. The FCC to BCC phase transformation can be illustrated by Fig. 4, where grain G3 and G4 (cf. Fig. 3) are the large and small grains, respectively. The phase transformation at the junction of grain G3 and G4, as indicated by the short arrow (cf. Fig. 3b), corresponds to the meeting of SF1 and SF2 near GB. At high strain rate (1×10^{10} s^{-1}), the FCC to BCC phase transformation inside the large grain (cf. Fig. 3e and f) corresponds to the intersection of SF2 and SF3 in Fig. 4. The above results can be ascribed to three points: (I) The low SFE of the HEA results in a large number of SFs. (II) It is easier to activate different slip directions under ultra-high strain rates. (III) Many dislocations can be accommodated in the big grain, and the propagation of phase transformation is caused by the interaction of dislocations with previously generated small BCC phase. Different to the numerous FCC to BCC phase transformation in large grain, the SFs are almost parallel to each other independent of different strain rates (5×10^7 and 1×10^{10} s^{-1}) in most small grains due to the suppressed cross-slip by the large separation between partial dislocations in HEAs with low SFE [11,43].

The total dislocation density under four strain rates can be calculated according to the following equation [44]:

$$\rho = \frac{L}{V} \tag{2}$$

where L is the length of dislocation and V is the volume of materials after deformation. The relevant result is plotted in Fig. 5. When $\varepsilon = 5\%–10\%$, the extremely rapid variation of total dislocation density (cf. Fig. 5a) and the percentage of BCC atomic groups (cf. Fig. 5b) under the strain rate of 1×10^{10} s^{-1} indirectly indicates that the intersected SFs occur earlier under ultra-high strain rate.

3.2. *The influence of Al concentration*

In this section, four simulation cells of $CoNiFeAl_xCu_{1-x}$ (x = 0.1, 0.2, 0.3 and 0.4, named M1, M2, M3 and M4, respectively) HEAs with the heterogeneous grain structure (D_G = 22 nm) are constructed and the uniaxial tensile simulation are performed along y axis. The phase stability can be effectively predicted by the mixing enthalpy [45–48]. When VEC ≥ 8, $-22 \le \Delta H_{mix} \le 7$ and $\delta \le 6.6\%$, the FCC solid solution phase can be regarded as stable, where ΔH_{mix} is mixing enthalpy, VEC is the valence electron concentration and δ is the misfit strain. They can be computed as [49]:

$$\Delta H_{mix} = \sum_{i=1, j\neq i}^{n} 4\Delta H_{ij}^{mix} c_i c_j \tag{3}$$

where ΔH_{ij}^{mix} is the enthalpy of mixing for a liquid binary alloy ij, c_i is the atom concentration.

$$VEC = \sum_{i=1}^{n} c_i (VEC)_i \tag{4}$$

where $(VEC)_i$ is the valence electron concentration of i^{th} alloy element [48].

$$\delta = \sqrt{\sum_{i=1}^{N} c_i \left(1 - \frac{r_i}{\left(\sum_{i=1}^{n} c_i r_i\right)}\right)^2} \tag{5}$$

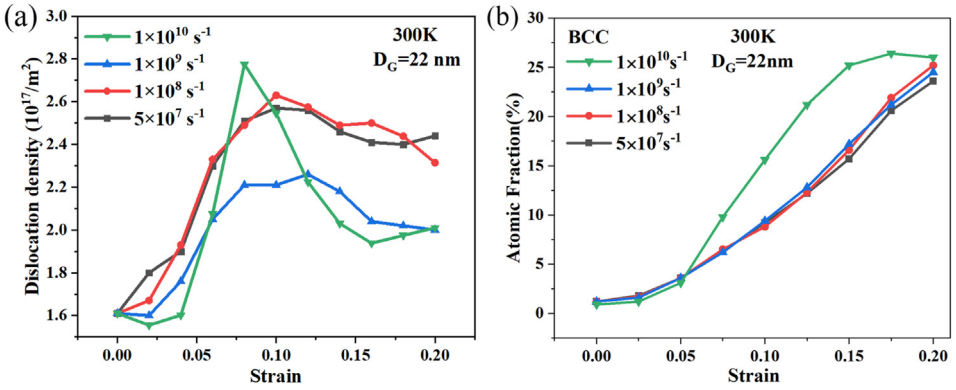

Fig. 5 – Dislocation density and BCC atomic fraction of heterogeneous grain structured $CoNiFeAl_{0.3}Cu_{0.7}$ HEA under different strain rates: (a) Total dislocation density versus strain; (b) Atomic fraction of BCC structure versus strain.

Table 1 – Atomic radius and VEC of each alloy element [48] and ΔH_{ij}^{mix} (kJ mol^{-1}) in binary equiatomic alloys [50].

Elements	Atomic radius(Å)	VEC	Co	Ni	Fe	Al	Cu
Co	1.251	9	\	0	−1	−19	12
Ni	1.246	10	0	\	−2	−22	4
Fe	1.241	8	−1	−2	\	−11	13
Al	1.432	3	−19	−22	−11	\	−1
Cu	1.278	11	12	4	13	−1	\

Table 2 – The values of mixing enthalpy (ΔH_{mix} (kJ/mol)), valence electron concentration (VEC) and misfit strain (δ) calculated by Eqs. (3)–(5).

Alloys	Identification	ΔH_{mix} (kJ mol^{-1})	VEC	δ (%)
$Co_{25}Ni_{25}Fe_{25}Al_{0.025}Cu_{0.225}$	M1	4.45	9.3	2.47
$Co_{25}Ni_{25}Fe_{25}Al_{0.05}Cu_{0.2}$	M2	2.41	9.1	3.29
$Co_{25}Ni_{25}Fe_{25}Al_{0.075}Cu_{0.175}$	M3	0.37	8.9	3.94
$Co_{25}Ni_{25}Fe_{25}Al_{0.1}Cu_{0.15}$	M4	−1.66	8.7	4.51

where r_i is the atomic radius of the individual alloy component. The values of ΔH_{ij}^{mix} of various atom pairs for Co, Ni, Fe, Al and Cu are provided with the VEC and the atomic radii in Table 1 and the theoretical calculations of ΔH_{mix}, VEC and δ are showed in Table 2.

The results of above calculations indicate that M1-M4 systems all have stable FCC structure. After relaxation, the FCC structure of M1-M4 remains stable. The average cohesive energy reduces from −4.049298 to −4.077305eV, indicating that the lower Al concentration, the more stable FCC HEA. Chen et al. [27] found that only FCC peak pattern was observed in $CoNiFeAl_xCu_{1-x}$ (x = 0.25 and 0.5), while both FCC and BCC structures were observed in $CoNiFeAl_{0.75}Cu_{0.25}$ alloy. Yeh et al. [1] also found that $CoCrNiFeAl_xCu_{1-x}$ (x from 0 to 0.5) presented only FCC peak pattern, while the BCC structure was observed when x is greater than 0.8. Above experiments demonstrated that the decrease of Al concentrations could improve the stability of FCC structure in HEA, which provided powerful data support for our simulations.

The uniaxial tensile stress–strain curves of M1-M4 are presented in Fig. 6. It can be found that the yield stress of $CoNiFeAl_xCu_{1-x}$ with heterogeneous structure has an approximately linear relation with Al concentration (cf. Fig. 6b). The yield stress of multi-principal alloys is decreased if the atom ratio is changed, because the lattice distortion energy is increased by raising the concentration of solid atoms. As a result, the SFE of HEA will decrease, thereby further reducing twin nucleation stress and the yield stress [51]. To measure the lattice distortion, the Von Mises stress of M1-M4 are calculated by the following formulation [52]:

$$\sigma_{Mises} = \sqrt{\frac{1}{2}\left[(\sigma_{xx}-\sigma_{yy})^2+(\sigma_{xx}-\sigma_{zz})^2+(\sigma_{yy}-\sigma_{zz})^2\right]+3\left(\sigma_{xy}^2+\sigma_{xz}^2+\sigma_{yz}^2\right)} \quad (6)$$

where σ_{xx}, σ_{yy}, σ_{zz}, σ_{xy}, σ_{xz} and σ_{yz} are the components of atomic stress. The Von Mises stress of atoms calculated using LAMMPS and outputted by OVITO software, are shown in Fig. 7a–h for simulation cells M1 and M4. The stress of the atoms in M4 (Fig. 7e–h) is generally greater than that in M1 (Fig. 7a–d) under any strain, especially when ε = 20%. In this case, the regions of high atomic stress (black circles) of M4 (cf. Fig. 7h) is significantly larger than that of M1 (cf. Fig. 7d). The number of atomic stress under different deformation stages are shown in Fig. 7i, and the sequence number of the curves correspond to Fig. 7(a–h). It can be seen that the curves of M4 under different strain (ε = 3%, 6%, 12.5% and 20%) are all above that of M1. Besides, the amount of scatter points corresponding to the low atomic stress of M1 (5–9 GPa) are obviously denser than those of M4, indicating that the degree of lattice distortion of $CoNiFeAl_xCu_{1-x}$ HEAs can be increased by raising the Al concentration. Generally speaking, solid solute atoms hinder the movement of dislocations so that solid solution hardening occurs in the dilute solid solutions [53,54]. However, the extra distortion energy generated by the high concentration of solid solutions atoms eventually lead to the reduction of twin nucleation stress in HEA systems [51]. As in some recent experiments [54,55], it was also found that the increase of large atomic radius element content can induce the fluctuation or decline of mechanical properties of HEA. The number of atoms with high atomic stress (≥25 GPa) at the yield stress point are presented in Fig. 7j. The curve is not linear, because the relative positions of various atoms change extremely fast under ultra-high strain rates, and the

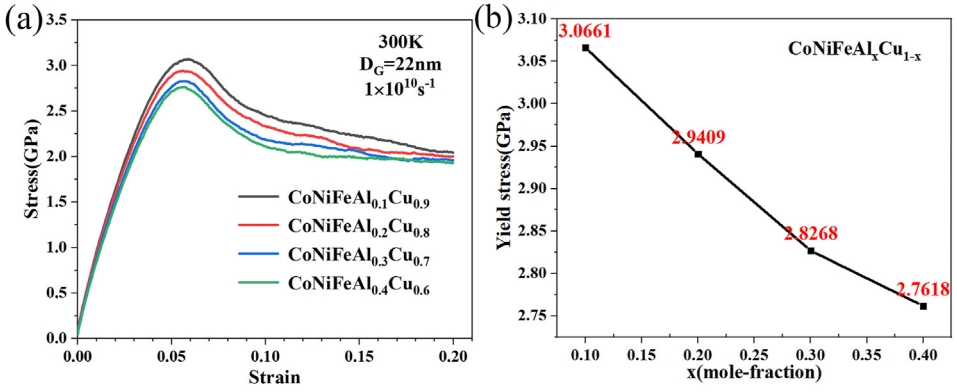

Fig. 6 – Stress–strain curves (a) and yield stress; (b) of heterogeneous grain structured $CoNiFeAl_xCu_{1-x}$ (x = 0.1, 0.2, 0.3 and 0.4).

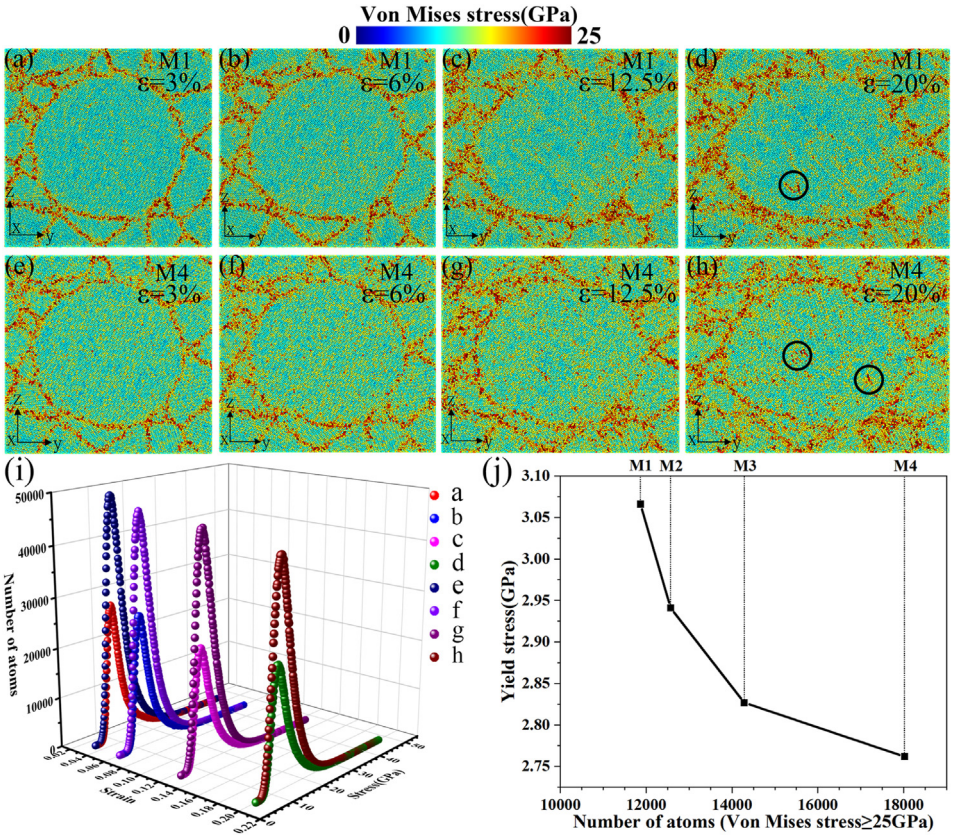

Fig. 7 – Distributions of σ_{Mises} in M1 and M4 with $D_G = 22$ nm at various strains under a strain rate of 1×10^{10} s^{-1}. (a)–(d) $CoNiFeAl_{0.1}Cu_{0.9}$ HEA (M1); (e)–(h) $CoNiFeAl_{0.4}Cu_{0.6}$ HEA (M4); (i) Number of atoms corresponding to the atomic stress in M1 and M4; (j) The number of atoms with high atomic stress at the yield stress point.

degree of lattice distortion continuously rises, especially in the system with high Al concentration (M3 and M4) [56].

Some experiments found that the reduction of stacking fault energy (SFE) can intensify the degree of phase transformation [48–50]. In order to explore the relationship between SFE and TRIP effect, in this work, six single crystal models of M1-M4, pure Ni and Cu ($12 \times 12 \times 20$ nm^3) were constructed. The x, y, and z axes of the simulation box were aligned with the [11-2], [-110] and [111] crystal directions, respectively. Periodic boundary conditions were enforced along x and y directions and free surface boundary condition was used in z direction. The top half of the crystal was displaced as a rigid body with respect to the bottom half in the negative x direction by a calculated value. Finally, the difference between the total energy after energy minimization and the energy of the initial configuration was counted. SFE was calculated using the following equation [35]:

$$E_s = (E_f - E_0)/A \quad (7)$$

where E_s is the SFE, E_f is the potential energy of the system after creating the SF, E_0 is the potential energy of the system before creating the stacking fault and A is the area of the stacking fault. The single crystal model M3 presented in Fig. 8d. Fig. 8a is the initial configuration, and the local potential energy is not minimized at this time. During the displacement, the microstructural evolutions of M3 are shown in Fig. 8a–c. Fig. 8b and c show the results of potential energy minimization after being moved a/6<11-2>. It can be found in the black rectangular frame (cf. Fig. 8a–c) that the atoms deviate from the initial points although they are indeed at the FCC points after energy minimization. As is shown in Fig. 8e, the derived stable SFE (γ_{sf}) corresponding to M1-M4 are 19.64, 13.44, 6.6 and 1.51 (mJ/m^2), respectively. Therefore, the increase of Al atoms could reduce the γ_{sf} of $CoNiFeAl_xCu_{1-x}$ HEAs. The fraction of each structure (FCC, BCC, HCP and other) and the snapshots of common neighbor analysis (CNA) are shown in Fig. 8f–h, which shows that the degree and variation speed of FCC to BCC transformation in M4 are higher than those of M1. Similarly, Fang et al. [25] found that CoCrFeMnNi HEA with dual-phase is easier to induce the HCP phase transformation and partial dislocation motion due to the low SFE. Yang et al. [57] also found that by increasing the degree of lattice distortion of $Fe_{45}Co_{30}Cr_{10}V_{10}Ni_{5-x}Mn_x$ HEAs, the reduction of SFE occurs. Meanwhile, the phase transformation is intensified during deformation. Besides, Voro++ package was used to calculated the free volume of M1 and M4 during deformation at strain rate equal to 10^{10} s^{-1} at 300 K [58]. As Fig. 8i shows, the free volume of M4 is bigger than that of M1, which represents that the tensile ductility of M4 will

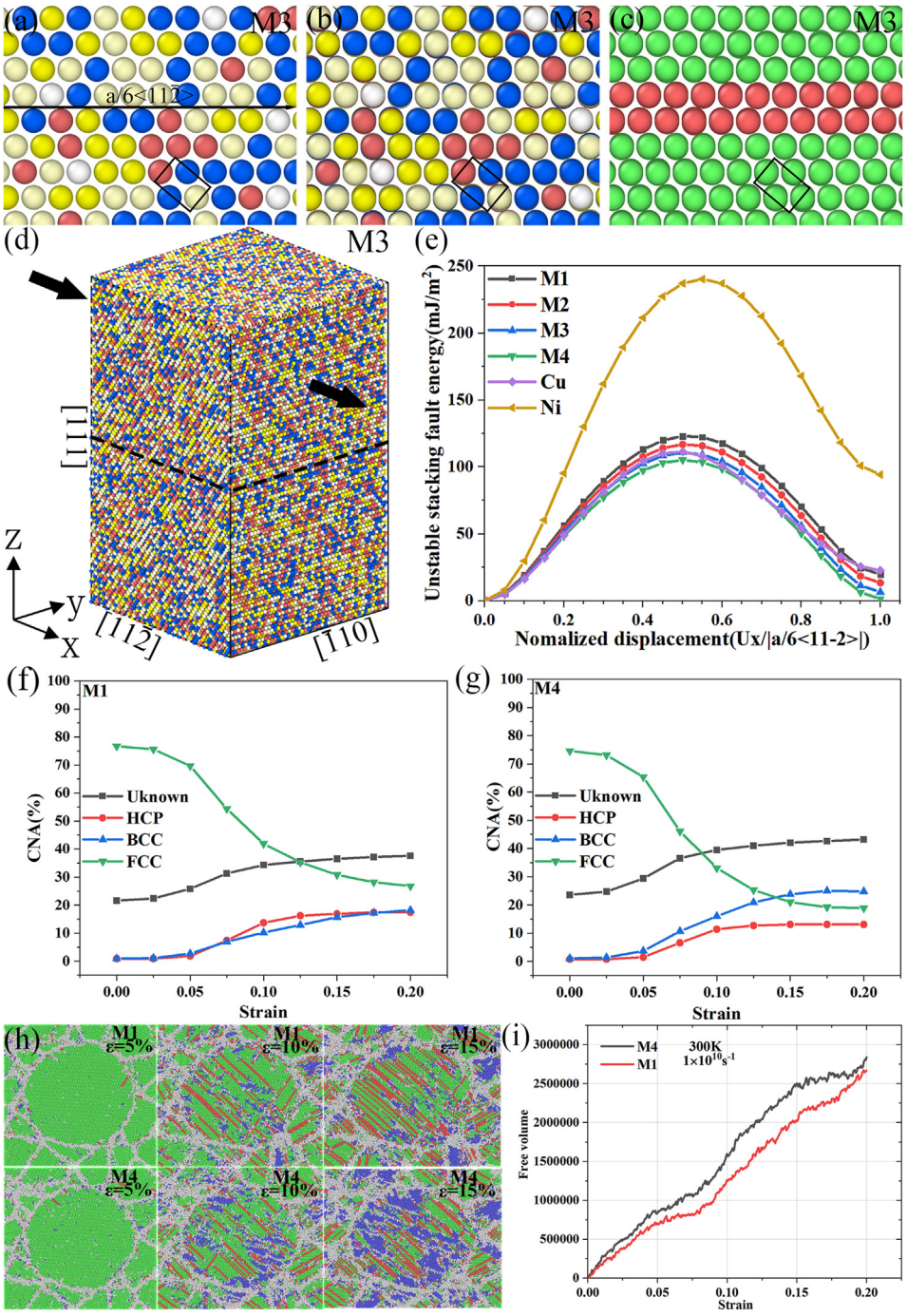

Fig. 8 – (a)–(c) The formation process of SF; (d) The orientation of single crystalline $CoNiFeAl_{0.3}Cu_{0.7}$; (e) Unstable SFE curves calculated for FCC HEAs (M1-M4), pure Ni and Cu; (f,g) Atomic fraction of different crystal structure during tensile deformation under the strain rate of 1×10^{10} s^{-1}; (h) Common neighbor analysis of M1 and M4 during deformation; (i) Free volume of M1 and M4 during tensile deformation.

be higher than M1. Therefore, the strain softening in Fig. 6a can also be partly attributed to the intensification of phase transformation caused by the increase of aluminum element concentration [59].

The dislocation analysis (DXA) algorithm was performed to characterize the dislocation evolution of M1 and M3. The region indicated by the yellow arrow is occupied by the BCC structure. Here, we only performed DXA on the FCC structure so that the BCC atoms (yellow region) was identified as defect mesh. It is precisely because these BCC structures are distributed in the grain interiors, which lead to the discrete distribution of partial dislocations. By observing the DXA of M1 and M3 (cf. Fig. 9a and b), it can be seen that the swing amplitude of the dislocation line is tremendous (cf. the red

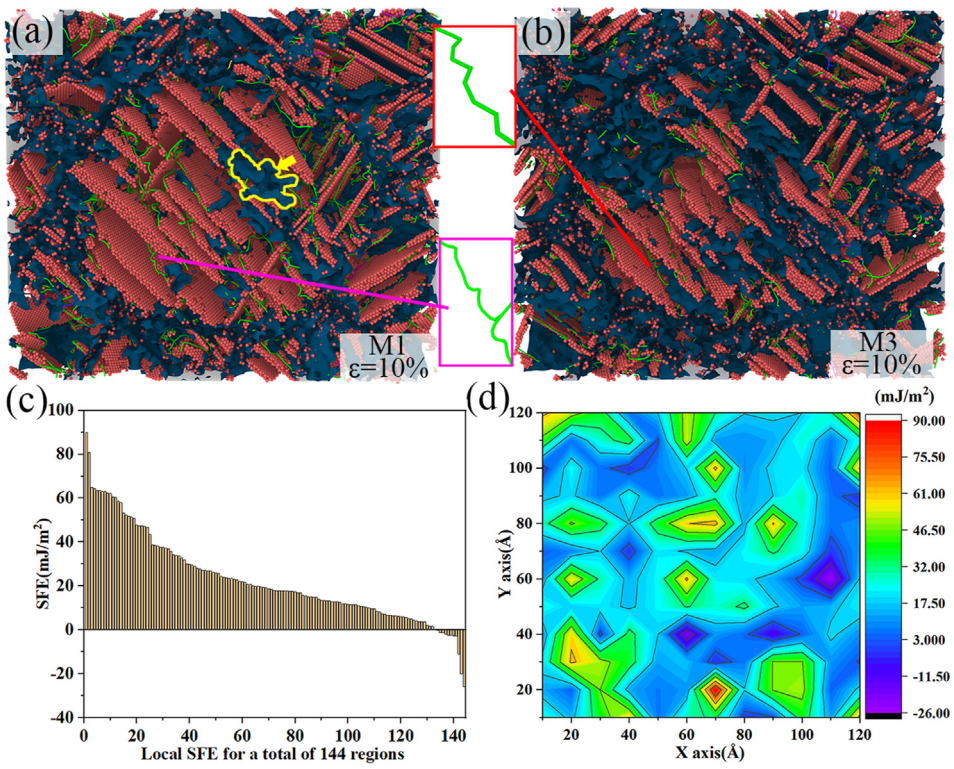

Fig. 9 – Dislocation analysis at the strain of 10% in (a) M1; (b) M3; (c) the SFEs of 144 independent calculations; (d) A local SFE landscape of M1.

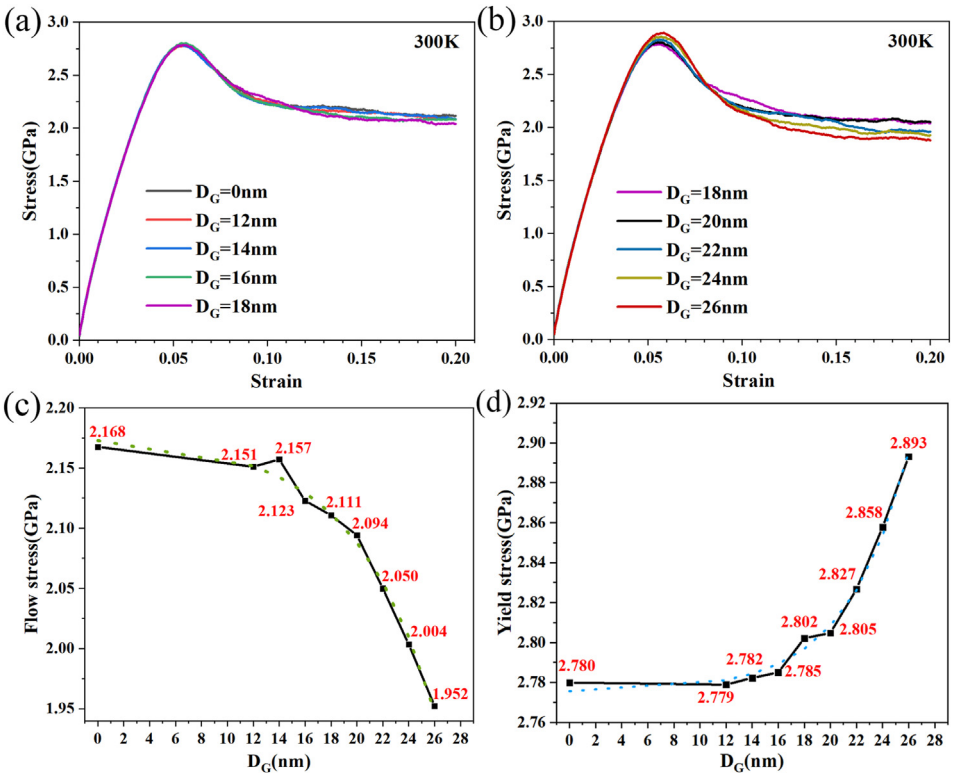

Fig. 10 – Stress–strain curves of heterogeneous grain structured $CoNiFeAl_{0.3}Cu_{0.7}$ HEA under strain rate of 1×10^{10} s^{-1} with (a) D_G from 0 to 18 nm; (b) D_G from 18 to 26 nm; (c) Flow stress versus the large grain size D_G from the simulation; (d) Yield stress at different D_G.

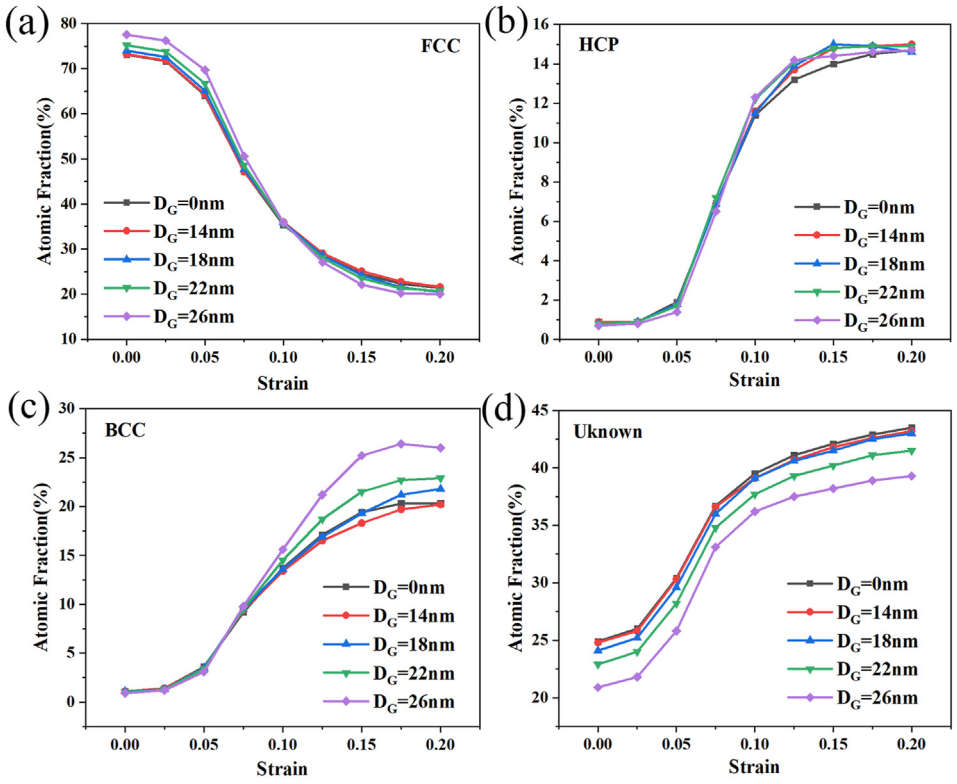

Fig. 11 – The atomic fraction of heterogeneous grain structured $CoNiFeAl_{0.3}Cu_{0.7}$ HEA with different D_G. (a) FCC atomic groups; (b) hcp atomic groups; (c) BCC atomic groups and (d) unknown atomic groups.

and pink rectangular local magnifying frame in Fig. 9). To explain this phenomenon, the slip plane of the model, which was used to calculate the SFE of M1 mentioned above, was divided (planar surface is 12 × 12 nm^2). The area was divided into 144 equal parts and the SFE of each part was calculated. The results of 144 independent SFE calculations are shown in Fig .9c and a local SFE landscape of M1 is presented in Fig .9d. Local inconsistency of SFEs causes the dislocations wavy slip pattern occurs. It is also observed by the experiment [60] that dislocation need to overcome the great difference in energy to complete the slip, which results in slow dislocation movement and dislocations attempt to bypass the high region of the barrier to complete the dislocation slip. According to the research reported by Lei et al. [5], the plastic flow can be homogenized when wavy slip pattern exists.

3.3. *Influence of grain heterogeneity on tensile properties*

To explore the influence of the grain heterogeneity on the tensile mechanical properties and phase transformation of FCC $CoNiFeAl_{0.3}Cu_{0.7}$ HEA, the D_G varies from 12 to 26 nm, while the average grain size of small grains is 9 nm. According to the study reported by Chen et al. [27], the transition value of Hall–Petch and inverse Hall–Petch relations is about 12.1 nm. Therefore, the sizes of large grains belong to the Hall–Petch relationship. In this section, the strain rate and temperature are set to 1 × 10^{10} s^{-1} and 300 K, respectively. Fig. 10a and b show the stress–strain curves of D_G (0–18 and 18–26 nm). It can be seen that the trend of the curves obviously changes when D_G = 18–26 nm (cf. Fig. 10b). With the variation of D_G, the yield stress of the model rises while average flow stress reduces. To distinguish the difference of flow stress, it is calculated as the average stress interval of 10–20%. As shown in Fig. 10c, the increase of D_G degrades the flow stress and it appears exponential decline relation. It can be partly attributed to the limitation of the box size and the enlargement of D_G, the region of small grains is compressed over a quite limited volume. This further caused that the average grain size of small grains declined, so the flow stress decreases with the refinement of small grains. Besides, when plastic deformation begins, the phase transformation gradually plays a crucial role, which leads to the relaxation of excess stress, as mentioned above. It is important to note that the size of average small grains is about 9 nm, which is lower than the Hall–Petch relationship explained above. The yield stress at different D_G is presented in Fig. 10d. Note that the yield stress of D_G = 0 nm is a little higher than that of D_G = 12 nm, because the unit cell with the small D_G has a large proportion of GB, resulting in greater dislocation propagation barriers. As a result, more energy is required to propagate the dislocation through the GB, which leads to the increase of yield stress. In addition, the yield stress rises with the increase of D_G (cf. Fig. 10d). It may be because the grain size of our simulation is much smaller than that of the experiment, and the volume of the simulation boxes is limited to 27,000 nm^3 due to in order to enhance the computational efficiency. Therefore, large grains have greater dominance of deformation during the linear

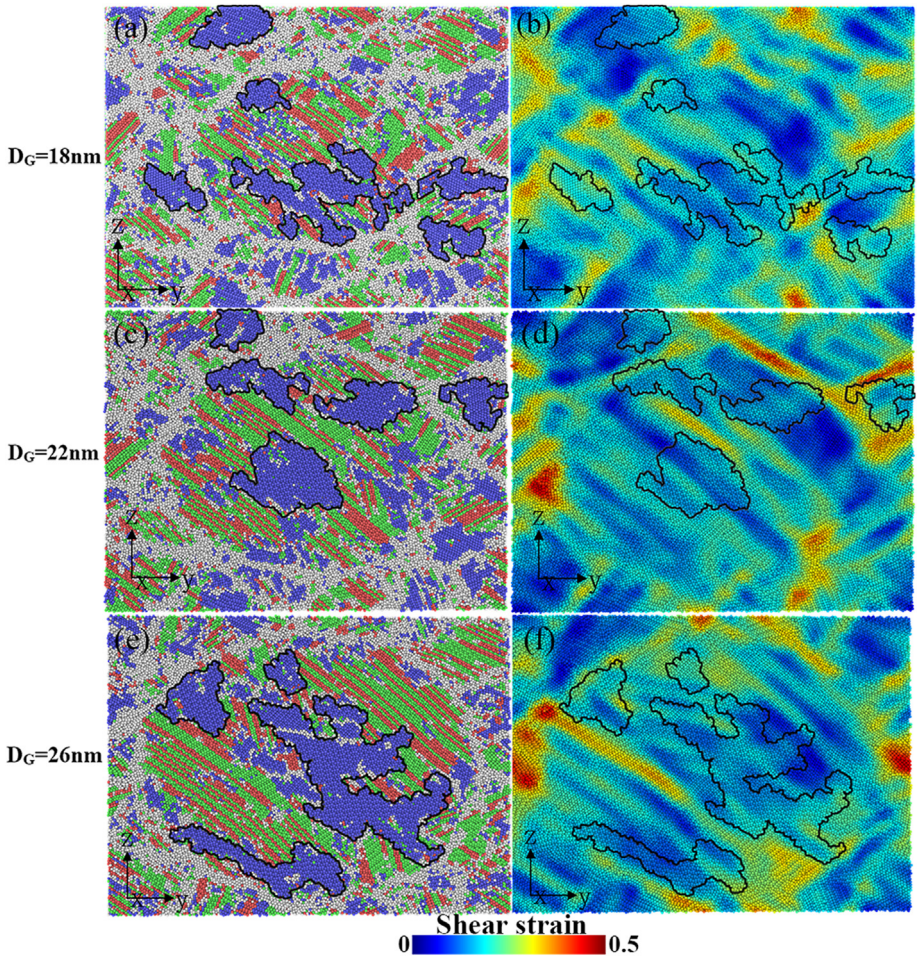

Fig. 12 – Common neighbor analysis of heterogeneous grain structured $CoNiFeAl_{0.3}Cu_{0.7}$ HEA with (a) $D_G = 18$ nm; (c) $D_G = 22$ nm and (e) $D_G = 26$ nm; Atomic strains in the HEA model with (b) $D_G = 18$ nm; (d) $D_G = 22$ nm and (f) $D_G = 26$ nm.

elastic stage with the D_G increases gradually, especially when the D_G approaches to the size of the simulation box. Besides, dislocations cannot be emitted in time in the case of extremely high strain rate, which leads to the bumps be more and more obvious in the stress–strain curves [61].

The evolution of FCC, HCP, BCC and unknown atomic groups of unit cells with various D_G as a function of strain are presented in Fig. 11. The atomic fraction of HCP decreases with increasing of D_G when the strain below 5% (cf. Fig. 11b), indicates that the dislocations are more difficult to emit from GB, which can further account for the reason for the difference in yield stress of the model with different D_G. Although the large grain size (D_G) affects the proportion of GB (cf. Fig. 11d), the model with the largest D_G has the smallest number of FCC structure atoms after $\varepsilon = 10\%$ (cf. Fig. 11a). Meanwhile, it can be seen obviously that the atomic fraction of BCC rises faster when the D_G is bigger (cf. Fig. 11c). Here, more than 20% of FCC structure transforms to the BCC structure. Because during the plastic deformation, the larger D_G has more region for SFs to intersect with each other at high strain rate, thus promoting an increase in FCC to BCC transformation, as mentioned in Section 3.1. It results in that the critical strain required to trigger the phase transformation decreases with the increasing of D_G. Besides, the volume fraction of phase transformation is proportional to the relaxation of stress in the plastic flow stage. Therefore, flow stress decreases as D_G increases, as showed in Fig. 10c. Further, Von Mises strain of different D_G (18, 22 and 26 nm) were calculated by OVITO, the local shear invariant of atom i can be calculated as follows [62]:

$$\varepsilon_i^{Mises} = \sqrt{\varepsilon_{xy}^2 + \varepsilon_{xz}^2 + \varepsilon_{yz}^2 + \frac{(\varepsilon_{xx} - \varepsilon_{yy})^2 + (\varepsilon_{xx} - \varepsilon_{zz})^2 + (\varepsilon_{yy} - \varepsilon_{zz})^2}{6}} \quad (8)$$

When the large grains occupy the space of models, more SF-SF intersection appears so that more significant phase transformation volume is induced (cf. Fig. 12a, c and e). It can be seen in Fig. 12b, d and f that FCC to BCC phase transformation can reduce the local strain of the alloy to enhance plasticity. However, the increase of tensile strain lead to compressive strain, which induces the softening in HEA, just like the study reported by Li et al. [22]. Besides, the large grain sizes D_G belong to Hall–Petch relationship, it is also a part of

reason for the flow stress decreases with the D_G increases in our simulations.

The grain size and the grain size ratio are much smaller in the MD simulations than those in the experiments due to the limitation of three-dimensional size. For this kind of heterogeneous grain structure of metal materials in the experiments [63], the size of the ultrafine grain is about 200 nm, while the grain size for the coarse grain is about several to dozens of μm. Therefore, the degree of grain heterogeneity in this nanoscale cannot reach that in macro concept. Considering an intuitive presentation, we simulated a heterogeneous grain structured HEA with large grain sizes of 26 nm and a homogeneous grain structured counterpart. In this simulation, periodic boundary condition was only applied along y direction. Therefore, there are free surfaces along the x and z directions to allow visual surface effects. The tensile simulation results show that the ductility of HEA with heterogeneous grain structure is remarkably improved (presented as a video in the Supplementary materials). Relying on the soft large grain, HEA with heterogeneous grain structure has more volume to share uniform plastic deformation than homogeneous nanocrystalline HEA.

Supplementary video related to this article can be found at https://doi.org/10.1016/j.jmrt.2021.07.116

4. Summary and conclusions

In this work, the tensile behavior of $CoNiFeAl_xCu_{1-x}$ HEA with heterogeneous structure was simulated at different strain rate, aluminum (Al) concentration and large grain sizes. The relevant deformation mechanisms have been explored. The combination of heterogeneous grain structured and strain softening mechanism provides insights into improving mechanical properties of HEAs. Based on the results of simulation, some conclusions can be drawn as follows:

(1) The increase of strain rate changed the deformation mechanisms of FCC $CoNiFeAl_{0.3}Cu_{0.7}$ with heterogeneous grain structure from grain combination and dislocation motion to GB diffusion and stacking fault (SF) interaction. Especially at the ultra-high strain rate (1×10^{10} s^{-1}), SF-SF intersection is more likely to occur in the large grains, resulting in a higher degree of phase transformation at high strain rate than at low strain rate (5×10^{7} s^{-1}). For small grains, the SFs are almost parallel to each other independent of different strain rates due to the suppressed cross-slip by the large separation between partial dislocations in HEAs with low SFE.

(2) The stable SFE values of 19.64, 13.44, 6.6 and 1.51 (mJ/m^2) were respectively obtained for FCC structured $CoNiFeAl_{0.1}Cu_{0.9}$, $CoNiFeAl_{0.2}Cu_{0.8}$, $CoNiFeAl_{0.3}Cu_{0.7}$ and $CoNiFeAl_{0.4}Cu_{0.6}$ HEAs. The yield stress of heterogeneous grain structure can be improved by decreasing the Al concentration. Besides, the degree of FCC to BCC phase transformation can be raised by the drop of SFE. Local non-uniform SFE lead to the great difference in energy that dislocation need to overcome to complete the slip, resulting in the occurrence of wiggled dislocation lines and slow dislocation movement.

(3) When the size of large grains increases, the plasticity of HEA is improved and the strength can be also guaranteed. The large grain shares much plastic strain, while the existence of FCC to BCC phase transformation makes the strain softening during plastic flow stage, which may bring about further enhance the ductility of HEAs.

Obvious grain rotation takes place in the small grains during the plastic deformation of heterogeneous grain structured HEAs. Grain rotation accommodates mechanical incompatibility and supports more plastic deformation. Theoretically, the back/forward stress between large and small grains may be beneficial to accelerate the behavior of grain rotation and this is worth further systematic discussion.

Declaration of Competing Interest

The authors declare no conflict of interest.

Acknowledgements

This work was supported by the Guizhou Provincial General Undergraduate Higher Education Technology Supporting Talent Support Program (KY(2018)043), the National Natural Science Foundation of China (,10502025 10872087, 11272143), the Program for Chinese New Century Excellent Talents in university (NCET-12-0712), the Key University Science Research Project of Jiangsu Province (17KJA130002), the National Key R&D Program of China (Grant No. 2017YFA0204403), National Natural Science Foundation of China (Grant No. 51971112 and 51225102), the Fundamental Research Funds for the Central Universities (Grant No. 30919011405), the Natural Science Foundation of Jiangsu Province (BK20201031), Scientific Research Fund for High-level Talents in Nanjing Institute of Technology (YKJ201952), Jiangsu Key Laboratory of Green Process Equipment (GPE202004) and the Postgraduate Research & Practice Innovation Program of Jiangsu Province (KYCX21_1131, SJCX21_0495).

REFERENCES

[1] Yeh J-W, Chen S-K, Lin S-J, Gan J-Y, Chin T-S, Shun T-T, et al. Nanostructured high-entropy alloys with multiple principal elements: novel alloy design concepts and outcomes. Adv Eng Mater 2004;6:299–303. https://doi.org/10.1002/adem.200300567.

[2] Cantor B, Chang ITH, Knight P, Vincent AJB. Microstructural development in equiatomic multicomponent alloys. Mater Sci Eng, A 2004;375–377:213–8. https://doi.org/10.1016/j.msea.2003.10.257.

[3] George EP, Raabe D, Ritchie RO. High-entropy alloys. Nat Rev Mater 2019;4:515–34. https://doi.org/10.1038/s41578-019-0121-4.

[4] Senkov ON, Miracle DB, Chaput KJ, Couzinie J-P. Development and exploration of refractory high entropy

alloys—a review. J Mater Res 2018;33:3092–128. https://doi.org/10.1557/jmr.2018.153.
[5] Lei Z, Liu X, Wu Y, Wang H, Jiang S, Wang S, et al. Enhanced strength and ductility in a high-entropy alloy via ordered oxygen complexes. Nature 2018;563:546–50. https://doi.org/10.1038/s41586-018-0685-y.
[6] Ding Q, Zhang Y, Chen X, Fu X, Chen D, Chen S, et al. Tuning element distribution, structure and properties by composition in high-entropy alloys. Nature 2019;574:223–7. https://doi.org/10.1038/s41586-019-1617-1.
[7] Zhang KB, Fu ZY, Zhang JY, Shi J, Wang WM, Wang H, et al. Annealing on the structure and properties evolution of the CoCrFeNiCuAl high-entropy alloy. J Alloys Compd 2010;502:295–9. https://doi.org/10.1016/j.jallcom.2009.11.104.
[8] Schneider M, George EP, Manescau TJ, Záležák T, Hunfeld J, Dlouhý A, et al. Analysis of strengthening due to grain boundaries and annealing twin boundaries in the CrCoNi medium-entropy alloy. Int J Plast 2020;124:155–69. https://doi.org/10.1016/j.ijplas.2019.08.009.
[9] Brechtl J, Chen SY, Xie X, Ren Y, Qiao JW, Liaw PK, et al. Towards a greater understanding of serrated flows in an Al-containing high-entropy-based alloy. Int J Plast 2019;115:71–92. https://doi.org/10.1016/j.ijplas.2018.11.011.
[10] Senkov ON, Wilks GB, Miracle DB, Chuang CP, Liaw PK. Refractory high-entropy alloys. Intermetallics 2010;18:1758–65. https://doi.org/10.1016/j.intermet.2010.05.014.
[11] Zhang Y, Zuo TT, Tang Z, Gao MC, Dahmen KA, Liaw PK, et al. Microstructures and properties of high-entropy alloys. Prog Mater Sci 2014;61:1–93. https://doi.org/10.1016/j.pmatsci.2013.10.001.
[12] Tsai K-Y, Tsai M-H, Yeh J-W. Sluggish diffusion in Co–Cr–Fe–Mn–Ni high-entropy alloys. Acta Mater 2013;61:4887–97. https://doi.org/10.1016/j.actamat.2013.04.058.
[13] Kashaev N, Ventzke V, Petrov N, Horstmann M, Zherebtsov S, Shaysultanov D, et al. Fatigue behaviour of a laser beam welded CoCrFeNiMn-type high entropy alloy. Mater Sci Eng, A 2019;766:138358. https://doi.org/10.1016/j.msea.2019.138358.
[14] Tang Z, Yuan T, Tsai C-W, Yeh J-W, Lundin CD, Liaw PK. Fatigue behavior of a wrought Al0.5CoCrCuFeNi two-phase high-entropy alloy. Acta Mater 2015;99:247–58. https://doi.org/10.1016/j.actamat.2015.07.004.
[15] Lv S, Zu Y, Chen G, Zhao B, Fu X, Zhou W. A multiple nonmetallic atoms co-doped CrMoNbWTi refractory high-entropy alloy with ultra-high strength and hardness. Mater Sci Eng, A 2020;795:140035. https://doi.org/10.1016/j.msea.2020.140035.
[16] Wu SW, Wang G, Wang Q, Jia YD, Yi J, Zhai QJ, et al. Enhancement of strength-ductility trade-off in a high-entropy alloy through a heterogeneous structure. Acta Mater 2019;165:444–58. https://doi.org/10.1016/j.actamat.2018.12.012.
[17] Naeem M, He H, Harjo S, Kawasaki T, Zhang F, Wang B, et al. Extremely high dislocation density and deformation pathway of CrMnFeCoNi high entropy alloy at ultralow temperature. Scripta Mater 2020;188:21–5. https://doi.org/10.1016/j.scriptamat.2020.07.004.
[18] Wang Y, Chen M, Zhou F, Ma E. High tensile ductility in a nanostructured metal. Nature 2002;419:912–5. https://doi.org/10.1038/nature01133.
[19] Schuh B, Pippan R, Hohenwarter A. Tailoring bimodal grain size structures in nanocrystalline compositionally complex alloys to improve ductility. Mater Sci Eng, A 2019;748:379–85. https://doi.org/10.1016/j.msea.2019.01.073.
[20] John R, Karati A, Joseph J, Fabijanic D, Murty BS. Microstructure and mechanical properties of a high entropy alloy with a eutectic composition (AlCoCrFeNi2.1) synthesized by mechanical alloying and spark plasma sintering. J Alloys Compd 2020;835:155424. https://doi.org/10.1016/j.jallcom.2020.155424.
[21] Xie L, Brault P, Thomann A-L, Bauchire J-M. AlCoCrCuFeNi high entropy alloy cluster growth and annealing on silicon: a classical molecular dynamics simulation study. Appl Surf Sci 2013;285:810–6. https://doi.org/10.1016/j.apsusc.2013.08.133.
[22] Li J, Fang Q, Liu B, Liu Y. Transformation induced softening and plasticity in high entropy alloys. Acta Mater 2018;147:35–41. https://doi.org/10.1016/j.actamat.2018.01.002.
[23] Afkham Y, Bahramyan M, Mousavian RT, Brabazon D. Tensile properties of AlCrCoFeCuNi glassy alloys: a molecular dynamics simulation study. Mater Sci Eng, A 2017;698:143–51. https://doi.org/10.1016/j.msea.2017.05.057.
[24] Choi W-M, Jo YH, Sohn SS, Lee S, Lee B-J. Understanding the physical metallurgy of the CoCrFeMnNi high-entropy alloy: an atomistic simulation study. npj Comput Mater 2018;4:1. https://doi.org/10.1038/s41524-017-0060-9.
[25] Fang Q, Chen Y, Li J, Jiang C, Liu B, Liu Y, et al. Probing the phase transformation and dislocation evolution in dual-phase high-entropy alloys. Int J Plast 2019;114:161–73. https://doi.org/10.1016/j.ijplas.2018.10.014.
[26] Lin Y, Yang T, Lang L, Shan C, Deng H, Hu W, et al. Enhanced radiation tolerance of the Ni-Co-Cr-Fe high-entropy alloy as revealed from primary damage. Acta Mater 2020;196:133–43. https://doi.org/10.1016/j.actamat.2020.06.027.
[27] Chen S, Aitken ZH, Wu Z, Yu Z, Banerjee R, Zhang Y-W. Hall-Petch and inverse Hall-Petch relations in high-entropy CoNiFeAlxCu1-x alloys. Mater Sci Eng, A 2020;773:138873. https://doi.org/10.1016/j.msea.2019.138873.
[28] Plimpton S. Fast parallel algorithms for short-range molecular dynamics. J Comput Phy 1995;117:1–19. https://doi.org/10.1006/jcph.1995.1039.
[29] Stukowski A. Visualization and analysis of atomistic simulation data with OVITO–the Open Visualization Tool. Model Simulat Mater Sci Eng 2010;18:015012. https://doi.org/10.1088/0965-0393/18/1/015012.
[30] Fu Z, Chen W, Wen H, Zhang D, Chen Z, Zheng B, et al. Microstructure and strengthening mechanisms in an FCC structured single-phase nanocrystalline Co25Ni25Fe25Al7.5Cu17.5 high-entropy alloy. Acta Mater 2016;107:59–71. https://doi.org/10.1016/j.actamat.2016.01.050.
[31] Zhou XW, Wadley HNG, Johnson RA, Larson DJ, Tabat N, Cerezo A, et al. Atomic scale structure of sputtered metal multilayers. Acta Mater 2001;49:4005–15. https://doi.org/10.1016/S1359-6454(01)00287-7.
[32] Zhou XW, Johnson RA, Wadley HNG. Misfit-energy-increasing dislocations in vapor-deposited CoFe/NiFe multilayers. Phys Rev B 2004;69:144113. https://doi.org/10.1103/PhysRevB.69.144113.
[33] Daw MS, Baskes MI. Embedded-atom method: derivation and application to impurities, surfaces, and other defects in metals. Phys Rev B 1984;29:6443–53. https://doi.org/10.1103/PhysRevB.29.6443.
[34] Sanchez JM, Vicario I, Albizuri J, Guraya T, Garcia JC. Phase prediction, microstructure and high hardness of novel light-weight high entropy alloys. J Mater Res Technol 2019;8:795–803. https://doi.org/10.1016/j.jmrt.2018.06.010.
[35] Wang CJ, Yao BN, Liu ZR, Kong XF, Legut D, Zhang RF, et al. Effects of solutes on dislocation nucleation and interface sliding of bimetal semi-coherent interface. Int J Plast 2020;131:102725. https://doi.org/10.1016/j.ijplas.2020.102725.
[36] Jiang W, Yuan S, Cao Y, Zhang Y, Zhao Y. Mechanical properties and deformation mechanisms of a

Ni2Co1Fe1V0.5Mo0.2 medium-entropy alloy at elevated temperatures. Acta Mater 2021;213:116982. https://doi.org/10.1016/j.actamat.2021.116982.
[37] Liu Y, Cao Y, Mao Q, Zhou H, Zhao Y, Jiang W, et al. Critical microstructures and defects in heterostructured materials and their effects on mechanical properties. Acta Mater 2020;189:129–44. https://doi.org/10.1016/j.actamat.2020.03.001.
[38] Horstemeyer MF, Baskes MI, Plimpton SJ. Length scale and time scale effects on the plastic flow of fcc metals. Acta Mater 2001;49:4363–74. https://doi.org/10.1016/S1359-6454(01)00149-5.
[39] Moosbrugger JC, Morrison DJ, Jia Y. Nonlinear kinematic hardening rule parameters Ð relationship to substructure evolution in polycrystalline nickel. Int J Plast 2000. 29.
[40] Zhang T, Zhou K, Chen ZQ. Strain rate effect on plastic deformation of nanocrystalline copper investigated by molecular dynamics. Mater Sci Eng, A 2015;648:23–30. https://doi.org/10.1016/j.msea.2015.09.035.
[41] Pu M, He Q, Zhou J. Molecular dynamic study on the deformation mechanism based on strain rate, solute atomic concentration and temperature in dual-phase equiaxial nanocrystalline AgCu alloy. J Alloys Compd 2019;795:241–53. https://doi.org/10.1016/j.jallcom.2019.04.304.
[42] Ma X, Huang C, Moering J, Ruppert M, Höppel HW, Göken M, et al. Mechanical properties of copper/bronze laminates: role of interfaces. Acta Mater 2016;116:43–52. https://doi.org/10.1016/j.actamat.2016.06.023.
[43] Zaddach AJ, Niu C, Koch CC, Irving DL. Mechanical properties and stacking fault energies of NiFeCrCoMn high-entropy alloy. JOM 2013;65:1780–9. https://doi.org/10.1007/s11837-013-0771-4.
[44] Ko W-S, Stukowski A, Hadian R, Nematollahi A, Jeon JB, Choi WS, et al. Atomistic deformation behavior of single and twin crystalline Cu nanopillars with preexisting dislocations. Acta Mater 2020;197:54–68. https://doi.org/10.1016/j.actamat.2020.07.029.
[45] Guo S, Liu CT. Phase stability in high entropy alloys: formation of solid-solution phase or amorphous phase. Prog Nat Sci: Mater Int 2011;21:433–46. https://doi.org/10.1016/S1002-0071(12)60080-X.
[46] Tian F, Varga LK, Chen N, Shen J, Vitos L. Empirical design of single phase high-entropy alloys with high hardness. Intermetallics 2015;58:1–6. https://doi.org/10.1016/j.intermet.2014.10.010.
[47] Troparevsky MC, Morris JR, Kent PRC, Lupini AR, Stocks GM. Criteria for predicting The formation of single-phase high-entropy alloys. Phys Rev X 2015;5:011041. https://doi.org/10.1103/PhysRevX.5.011041.
[48] Guo S, Ng C, Lu J, Liu CT. Effect of valence electron concentration on stability of fcc or bcc phase in high entropy alloys. J Appl Phys 2011;109:103505. https://doi.org/10.1063/1.3587228.
[49] Yang X, Zhang Y. Prediction of high-entropy stabilized solid-solution in multi-component alloys. Mater Chem Phys 2012;132:233–8. https://doi.org/10.1016/j.matchemphys.2011.11.021.
[50] Takeuchi A, Inoue A. Classification of bulk metallic glasses by atomic size difference, heat of mixing and period of constituent elements and its application to characterization of the main alloying element. Mater Trans 2005;46:2817–29. https://doi.org/10.2320/matertrans.46.2817.
[51] Li W, Fan H, Tang J, Wang Q, Zhang X, El-Awady JA. Effects of alloying on deformation twinning in high entropy alloys. Mater Sci Eng, A 2019;763:138143. https://doi.org/10.1016/j.msea.2019.138143.
[52] Huang C, Peng X, Zhao Y, Weng S, Yang B, Fu T. Flow strength limit of nanocrystalline tantalum predicted with molecular dynamics simulations. Mater Sci Eng, A 2018;738:1–9. https://doi.org/10.1016/j.msea.2018.09.053.
[53] Leyson GPM, Curtin WA, Hector LG, Woodward CF. Quantitative prediction of solute strengthening in aluminium alloys. Nat Mater 2010;9:750–5. https://doi.org/10.1038/nmat2813.
[54] Stanford N, Barnett MR. Solute strengthening of prismatic slip, basal slip and twinning in Mg and Mg–Zn binary alloys. Int J Plast 2013;47:165–81. https://doi.org/10.1016/j.ijplas.2013.01.012.
[55] Raza A, Ryu HJ, Hong SH. Strength enhancement and density reduction by the addition of Al in CrFeMoV based high-entropy alloy fabricated through powder metallurgy. Mater Des 2018;157:97–104. https://doi.org/10.1016/j.matdes.2018.07.023.
[56] Yaakobi B, Boehly TR, Meyerhofer DD, Collins TJB, Remington BA, Allen PG, et al. EXAFS measurement of iron bcc-to-hcp phase transformation in nanosecond-laser shocks. Phys Rev Lett 2005;95:075501. https://doi.org/10.1103/PhysRevLett.95.075501.
[57] Yang J, Jo YH, Kim DW, Choi W-M, Kim HS, Lee B-J, et al. Effects of transformation-induced plasticity (TRIP) on tensile property improvement of Fe45Co30Cr10V10Ni5-xMnx high-entropy alloys. Mater Sci Eng, A 2020;772:138809. https://doi.org/10.1016/j.msea.2019.138809.
[58] Tanemura M, Ogawa T, Ogita N. A new algorithm for three-dimensional voronoi tessellation. J Comput Phys 1983;51:191–207. https://doi.org/10.1016/0021-9991(83)90087-6.
[59] Diao JK, Gall K, Dunn ML. Surface-stress-induced phase transformation in metal nanowires. Nat Mater 2003;2:656–60. https://doi.org/10.1038/nmat977.
[60] Bu Y, Peng S, Wu S, Wei Y, Wang G, Liu J, et al. Unconventional deformation behaviours of nanoscaled high-entropy alloys. Entropy 2018;20:778. https://doi.org/10.3390/e20100778.
[61] Dong S, Chen T, Huang S, Li N, Zhou C. Thickness-dependent shear localization in Cu/Nb metallic nanolayered composites. Scripta Mater 2020;187:323–8. https://doi.org/10.1016/j.scriptamat.2020.06.049.
[62] Shimizu F, Ogata S, Li J. Theory of shear banding in metallic glasses and molecular dynamics calculations. Mater Trans 2007;48:2923–7. https://doi.org/10.2320/matertrans.MJ200769.
[63] Zhao Y, Topping T, Bingert JF, Thornton JJ, Dangelewicz AM, Li Y, et al. High tensile ductility and strength in bulk nanostructured nickel. Adv Mater 2008;20:3028–33. https://doi.org/10.1002/adma.200800214.